



Force transmission and anisotropic characteristics of sheared granular materials with rolling resistance

Wei Wu¹ · Gang Ma¹ · Wei Zhou¹ · Di Wang¹ · Xiaolin Chang¹

Received: 23 August 2018 / Published online: 22 August 2019
© Springer-Verlag GmbH Germany, part of Springer Nature 2019

Abstract

We adopt a two-dimensional granular assembly in a direct shear box to systematically investigate the role of rolling resistance during the shearing process. A discrete element method with parallel computation and a rolling friction model is utilized in this paper. The macro- and microscale responses are sensitively subjected to a change in the rolling friction. The critical-state indices are found to be linearly related to each other, and the linear relationship between the critical-state indices and the rolling friction coefficient is evidently observed. The macro- and microscopic relationships are discussed from the connections between the stress and fabric properties. For microscale behaviors, different rolling frictions can generate various magnitudes of arching effects caused by antirotation and pose different characteristics to the force chains. The algorithm related to the extraction of force chains is adopted to explain the local sustaining structures. The localization, length, number and magnitude distribution of the force chains depend on the rolling friction. The influence of the rolling resistance on the friction mobilization is evident. A transition of the force distribution from the exponential to the Gaussian distribution is observed when the rolling resistance conditions change. The strong–weak contact systems and various anisotropic parameters are utilized to characterize the mechanical and geometrical roles of rolling resistance.

Keywords Direct shear · DEM · Rolling friction · Critical state · Force chain · Anisotropy

1 Introduction

When simulating real granular materials in a direct shear test, incorporating the rolling resistance into a mechanical analysis is an effective approach but should still be systematically investigated. Ai et al. [1] summarized that rolling resistance arises from the following sources: microslip and friction on the contact surface, plasticity, deformation,

contacts, viscosity, hysteresis, and adhesion effects. They further comprehensively evaluated the performance of existing rolling resistance models [2–6] and noted the different models' limitations in specific applications. The irregularities or asperities of the granular surface can result in a weak rolling resistance, and a larger rolling resistance can be derived from interlocking between the grains with non-convex or angular shapes [7]. To some extent, utilizing the rolling resistance model can effectively reflect the influence of the particle shape on the particle interaction and geometrical arrangement.

Several authors have conclusively shown that the macro- and grain-scale responses are significantly affected by the particle's rolling resistance [8–11]. Estrada et al. [9] verified the validity of using rolling resistance as a shape parameter to account for particle angularity and proved that the hindrance of rotation acts as one of the main influencing factors in the mechanical behavior of granular systems. To recognize the authentic properties of using rotational resistance, Zhao and Guo [12] employed a triaxial compression test to investigate the influence of antirotation on the characteristic behavior of granular materials. However, both the macro-

✉ Gang Ma
magang630@whu.edu.cn

Wei Wu
wu_wei@whu.edu.cn

Wei Zhou
zw_mxx@whu.edu.cn

Di Wang
wangdi1010@whu.edu.cn

Xiaolin Chang
changxl@whu.edu.cn

¹ State Key Laboratory of Water Resources and Hydropower Engineering Science, Wuhan University, 430072 Wuhan, China

meso-, and micromechanical responses of the direct shear tests that consider rolling resistance still lack a comprehensive explanation from certain fundamental aspects.

A direct shear test is one of the most commonly used testing methods in geotechnical engineering [13]. Despite the limitations of the direct shear test, especially its nonuniform distribution of stresses and strains [14, 15], Potts et al. [16] confirmed that a granular assembly behaves uniformly within the final failure zone, with no significant development of the progressive failure, and that the peak strength prediction is accurate. It has been found that simple shear is the dominant deformation mode in the plane shear flows, the localized failure zones, and the shaking level grounds under seismic shear waves [17]. Dounias and Potts [18] also used the finite element method to demonstrate that the stress condition within the direct shear is analogous to the simple shear. The effectiveness of the two-dimensional discrete element modeling of direct shear tests was also illustrated [19]. A quantitative validation of the numerical modeling was performed by means of physical test data [20]. Similar to the discrete element method (DEM) simulations performed by Liu et al. [21], a simple shear region is selected at the center of the direct shear sample to extract the mechanical information, thus avoiding the inhomogeneous restraints of the boundary walls and facilitating more uniform fields of strain and stress for further study.

In terms of the microscopic levels, different shear zones are extracted to explore the local structural characteristics, and the relationship between the macro- and micro-scale properties are established. It is also observed that the micro-scale arching effect related to antirotation between particle contacts evidently influences the force chain behavior and local structures. The adequate algorithm to extract the force chains are realized in our work. In contrast to the crystalline or polycrystalline solids, the contact forces occupy an inhomogeneous distribution for packing granular materials.

Hence, the characterization of the force distribution in a granular medium is of great practical importance [22]. The jamming structures of particle assemblies [22] are also explored by means of the statistical method and force-chain characteristics. The strain localization corresponding to the shearing process is also figured out within different zones of the sample, and the properties of the nonaffine deformation are explored. For Hertzian potentials, the normal contact force distributions exhibit an exponential tail for large contact forces [23]. In this work, the transition between the exponential and Gaussian dependence of the probability distribution functions (PDFs) is discussed. To combine the multiscale properties, the correlation between the macroscopic and microscopic parameters is comprehensively investigated from various aspects. The basic theoretical backgrounds related to the rolling friction models and stress-force-fabric features are presented in Sect. 2. The open-source code LIGGGHTS [24] with the parallel computing method is employed in this paper. The implementation of the rotational resistance model put forward by Ai et al. [1] is coupled in the code.

2 Theoretical analysis

2.1 Rolling friction

The rolling of particles is an important factor for controlling the mechanism of fabric reconstruction [25]. Based on the model proposed by Iwashita [2] and Jiang et al. [6], Jun Ai et al. [1] used both one-way and cyclic rolling in the elastic–plastic spring-dashpot models. In this model, the total rolling resistance torque M_r contains a spring torque M_r^k and a viscous damping torque M_r^d . The mechanism of the loading and unloading behavior of the spring torque M_r^k is shown in Fig. 1. The incremental calculating procedure of

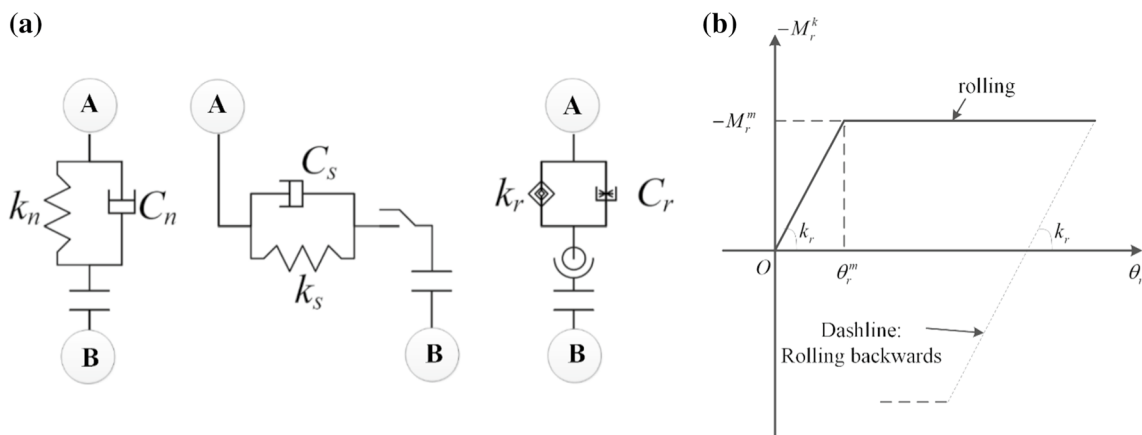


Fig. 1 a Contact model considering rolling friction [1]; b The mechanism of the loading and unloading behavior of the rolling resistance torque

the rolling torque is also adopted. The incremental equations are as follows:

$$\begin{aligned} \Delta M_r^k &= -k_r \Delta \theta_r \\ M_{r,t+\Delta t}^k &= M_{r,t}^k + \Delta M_r^k \\ |M_{r,t+\Delta t}^k| &\leq M_r^m \end{aligned} \tag{1}$$

where $M_r^m = \mu_r R_r f_n$ ($R_r = r_A r_B / (r_A + r_B)$ and f_n denotes the normal contact force) represents the limiting spring torque when the full mobilization rolling angle ($\theta_r^m = M_r^m / k_r$) is achieved. The rolling stiffness ($k_r = 3k_n \mu_r^2 R_r^2$) is used for calculations in this paper.

The viscous damping torque M_r^d is given by the following expression:

$$M_{r,t+\Delta t}^d = \begin{cases} -C_r \dot{\theta}_r, & \text{if } |M_{r,t+\Delta t}^k| < M_r^m \\ -f C_r \dot{\theta}_r, & \text{if } |M_{r,t+\Delta t}^k| = M_r^m \end{cases} \tag{2}$$

The rolling viscous damping coefficient C_r takes the form:

$$C_r = \eta_r C_r^{crit} \tag{3}$$

where η_r is the rolling viscous damping ratio and C_r^{crit} is the rolling critical viscous damping constant ($C_r^{crit} = 2\sqrt{I_r k_r}$). The term I_r is the equivalent moment of inertia for the relative rotational vibration mode between spherical particles:

$$I_r = \left(\frac{1}{J_A + m_A r_A^2} + \frac{1}{J_B + m_B r_B^2} \right)^{-1} \tag{4}$$

in which J_A and J_B are the moments of inertia corresponding to the centroid and m_A and m_B represent the masses of particles A and B , respectively. To analyze a single role of the rolling resistance coefficient, the values of η_r in Eq. (3) and f in Eq. (2) are set to zero in this paper.

2.2 Mechanical expressions in two-dimensional systems

2.2.1 Fabric and contact force description

The concept of ‘‘fabric,’’ which is used to describe the geometrical property of discontinuity in granular materials, was proposed by Oda [26]. The microscopic pictures of packed particles are attributed to three aspects: the mechanical roles of particle sliding and rolling during deformation, the mechanism of generating a shear plane, and the mechanism utilized to control the fabric reconstruction. For infinite assemblies in a two-dimensional system, the fabric tensor can be expressed in the general form [27, 28]:

$$F_{ij} = m_v \int_S E(\mathbf{n}) n_i n_j d\mathbf{n} \tag{5}$$

which also has a general normalized form [29]:

$$F_{ij} = \frac{1}{2N} \sum_{k=1}^{2N} n_i^k n_j^k \tag{6}$$

The term m_v is equal to $2N/S$ and represents the contact density (where S is the area of overall granular assembly and N denotes the number of contacts). The term $E(\mathbf{n})$, which characterizes the distribution of normal contact orientation, is visualized as the general 2D expression:

$$E(\theta) = \frac{\pi}{2} (1 + a_{ij}^c n_i n_j), \quad a_{ij}^c = a_{ji}^c, \quad a_{kk}^c = 0 \tag{7}$$

The anisotropic tensor, a_{ij}^c , can be calculated by the measured statistics of Eqs. (5) and (7):

$$a_{ij}^c = 4(F_{ij} - \frac{1}{2} \delta_{ij}) \tag{8}$$

and represents the deviatoric part of the tensor that characterizes the distribution of the overall normal contact orientation.

Using the second Fourier series expression, an approximation for the normalized normal contact direction is generated:

$$E(\theta) = \frac{\pi}{2} (1 + a_c \cos 2(\theta - \theta_c)) \tag{9}$$

The parameter a_c corresponds to a nondimensional coefficient characterizing the magnitude of the normal contact anisotropy, which is derived from the fabric tensor F_{ij} [30]:

$$a_c = \frac{2\sqrt{(F_{11} - F_{22})^2 + 4F_{12}^2}}{F_{11} + F_{22}} \tag{10}$$

The major principal direction of the normal contact anisotropy, θ_c , is expressed as

$$\theta_c = \frac{1}{2} \tan^{-1} \left(\frac{2F_{21}}{F_{11} - F_{22}} \right) \tag{11}$$

The distributions of the average normal and tangential force components can also be characterized by the average normal contact force tensor N_{ij} and the average tangential contact force tensor T_{ij} in the discrete or integral form [31], in a manner analogous to that of calculating the fabric tensor F_{ij} . Furthermore, both the anisotropy magnitude and preferred orientation of the mean contact forces can be derived from the tensors. The approximate equations of the tensors are the following:

$$N_{ij} = \frac{1}{2\pi} \int_0^{2\pi} \bar{f}_n(\theta) n_i n_j d\theta \approx \frac{1}{N_g} \sum_{\Delta\theta_g} \bar{f}_n^c n_i n_j \tag{12}$$

$$T_{ij} = \frac{1}{2\pi} \int_0^{2\pi} \bar{f}_t(\theta) t_i n_j d\theta \approx \frac{1}{N_g} \sum_{\Delta\theta_g} \bar{f}_t^c t_i n_j$$

The quotient N_g , which represents the number of orientation intervals, is 36 in this paper. The contact-based tangential directional vector ($\mathbf{t} = (-\sin \theta, \cos \theta)$) is orthogonal to the normal vector ($\mathbf{n} = (\cos \theta, \sin \theta)$). Here, the Fourier series expressions of both the average normal force component \bar{f}_n and the average tangential force component \bar{f}_t are put forward by Rothenburg [32]:

$$\begin{aligned} \bar{f}_n(\theta) &= \bar{f}_0[1 + a_n \cos 2(\theta - \theta_n)] \\ \bar{f}_t(\theta) &= \bar{f}_0[a_w - a_t \cos 2(\theta - \theta_t)] \end{aligned} \tag{13}$$

The term \bar{f}_0 , which characterizes the average normal contact force over all contacts in the assembly, is calculated by:

$$\bar{f}_0 = \frac{1}{2\pi} \int_0^{2\pi} \bar{f}_n(\theta) d\theta \tag{14}$$

The coefficients a_n , a_t and a_w are adopted to describe the anisotropy magnitude of \bar{f}_n and \bar{f}_t . The terms θ_n and θ_t are used to describe the principal orientation of the mean normal contact force $\bar{f}_n(\theta)$ and mean contact tangential force $\bar{f}_t(\theta)$, respectively. Similar to the procedure used in Eqs. (10) and (11), the parameters a_n , a_t , θ_n and θ_t can be calculated:

$$\begin{aligned} a_n &= \frac{2\sqrt{(N_{11} - N_{22})^2 + 4N_{12}^2}}{N_{11} + N_{22}}, & \theta_n &= \frac{1}{2} \tan^{-1}\left(\frac{2N_{21}}{N_{11} - N_{22}}\right) \\ a_t &= \frac{2\sqrt{(T_{11} - T_{22})^2 + 4T_{12}^2}}{N_{11} + N_{22}}, & \theta_t &= \frac{1}{2} \tan^{-1}\left(\frac{2T_{21}}{T_{11} - T_{22}}\right) \end{aligned} \tag{15}$$

Physically speaking, when the distribution of the tangential contact forces is not symmetrical, the value of a_w is nonzero, and it acts to compensate for a lack of the normal contact in the direction of maximum loading [31]. Under the moment equilibrium condition:

$$\int_0^{2\pi} \bar{f}_t(\theta) E(\theta) d\theta = 0 \tag{16}$$

The following expression for a_w is obtained:

$$a_w = \frac{1}{2} a a_t \sin 2(\theta_c - \theta_t) \tag{17}$$

2.2.2 Stress-fabric-force (S-F-F) relationship in 2D system

Granular assemblies sustain external pressure by redistributing them among the particle contacts. In an attempt to measure the fabric with a finite number of circular particles and a narrow size-distribution in a two-dimensional system, Rothenburg and Bathurst [30] expressed the average stress tensor throughout a granular assembly as [33–35]:

$$\sigma_{ij} = \frac{1}{S} \sum_{c \in S} f_i^c l_j^c \tag{18}$$

where S represents the area of a two-dimensional system and the sum is performed over all contacts. l_j represents the j th projection of the branch vector \mathbf{l} . Similar to the truncated Fourier series expressions of \bar{f}_n and \bar{f}_t , the mean of the branch vectors can be adopted as the function of the normal contact orientation:

$$\begin{aligned} \bar{d}_n(\theta) &= \bar{d}_0[1 + a_d \cos 2(\theta - \theta_d)] \\ \bar{d}_t(\theta) &= \bar{d}_0[a_d^w - a_d^t \sin 2(\theta - \theta_d)] \end{aligned} \tag{19}$$

The term \bar{d}_0 characterizes the mean length of the branch vectors in the assembly. The parameters a_d , a_d^w , and a_d^t symbolize the magnitude of anisotropy. Owing to the condition that the particle shape used in the paper is spherical, the value of $\bar{d}_t(\theta)$ equals zero.

The stress-force-fabric relationship (S-F-F) [30, 31, 36] in cohesionless granular assemblies provides an approach for bridging the gap between the macroscopic stress tensor and the microscopic anisotropic fabric parameters. The separate contributions of the normal contact force component, contact tangential force component, and normal contact component to the shear strength are discussed in several previous studies [37–40]. According to the distribution functions of $E(\theta)$, $\bar{f}_n(\theta)$, $\bar{f}_t(\theta)$ and $\bar{d}_n(\theta)$, the stress expression in Eq. (18) can be calculated by:

$$\sigma_{ij} = m_c \bar{d}_0 \int_0^{2\pi} [\bar{f}_n(\theta) n_i + \bar{f}_t(\theta) t_i][\bar{d}_n(\theta) n_j][1 + a_c \cos 2(\theta - \theta_c)] d\theta \tag{20}$$

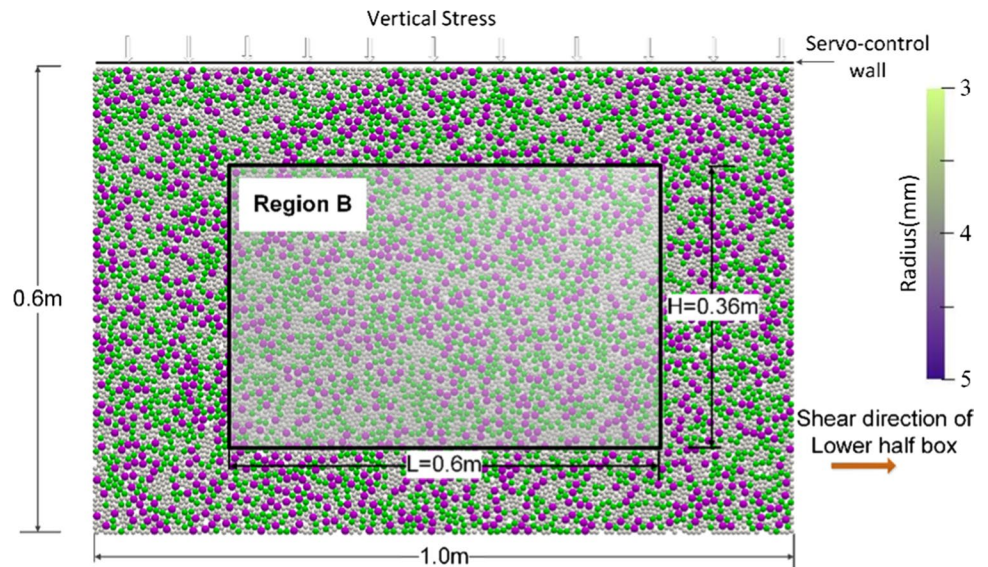
Hence, the stress tensor becomes the function of the anisotropy parameters, which ensures both the qualitative and quantitative connection of micro- and macroscale properties.

3 Numerical preparation

In the numerical simulation, the Hertz-Mindlin model is adopted as the contact law. Both the normal and tangential components have a spring force and a damping force. The tangential overlap is truncated to fulfill the Coulomb criterion $f_t \leq \mu f_n$. For the tangential force, there exists a “history” effect that can account for the tangential displacement between the particles as they contact each other. The model parameters involved in the computational procedure, such as the viscoelastic damping constants γ_n , γ_t and the elastic constants k_n , k_t , can be calculated via Young’s modulus E , the shear modulus G , the Poisson ratio ν , the coefficient of restitution e , and other quantities [41].

The initial direct shear box shown in Fig. 2 is 1.0 m long and 0.6 m high. The samples are composed of 10,000

Fig. 2 The characters of the granular assembly within direct shear tests



particles, with a linear radius distribution of 3, 4, and 5 mm, and particles with the same radii have the same mass percentage in the assembly. The radius expansion method is employed to generate a homogeneous numerical sample. This method is utilized to insert a specified number of particles with random coordinates in a predetermined space. Allowing for the fact that no new particles will be placed if the new particle overlaps with another particle or wall, an artificial small-radius particle swarm within the specified volume is created. The particles are then expanded until the required void ratio is obtained. Once the generation process is finished, the granular assembly is relaxed to release the overlaps under the confinement of a boundary produced by rigid walls with an infinite mass.

The initial sample comes to equilibrium with the movement of the four enclosed stress-servo-control walls. The coefficients of interparticle sliding friction and rolling friction are set to 0.5 and 0.0 during the sample preparation, respectively. During the shearing process, the sliding friction coefficient μ is then set to 0.5. The shearing is achieved by moving the lower half of the box to the right at a constant velocity accompanied with the constant vertical stress σ_{yy} . In this paper, the mean pressure for initial consolidation and the vertical stress during shearing are both set as 200 kPa, thus omitting the effect of the mean pressure from the following analysis.

To evaluate the mechanical role of rolling resistance, various rolling friction coefficients μ_r are used. Sixty-three simulations with a broad range of friction coefficients were performed to confirm the accuracy of the numerical results. The particle-wall rolling and sliding friction coefficients are set at 0.0 during both the consolidation and shearing process. To satisfy the condition of a quasistatic state during the simulation procedure, the horizontal strain rate is selected

to ensure the resulting inertia index $I = \dot{\epsilon}_x \langle d \rangle \sqrt{\rho/p} \leq 10^{-3}$ [42]. The horizontal velocity of the lower half of the box is set to 0.01 m/s, and the calculated strain ratio fulfill the quasi-static condition. The principal parameters taken in the DEM analysis are shown in Table 1.

In the direct shear test, the shear plane and the zero linear extension direction are horizontal [43, 44]. Because both the deformation and stresses in the central region of the sample are relatively uniform and exhibit a nearly simple shear mode, it has been concluded that the stress ratio and volumetric strain calculated from the simple shear region nearly coincide with those calculated from the entire sample used for the direct shear test [21, 45]. Hence, we also utilize this region to extract the microscopic information. Similarly, we adopted the displacement of the top servo-control wall to evaluate the volumetric behavior in this paper. In this study,

Table 1 Parameters for DEM simulation

Parameter	Symbol	Value	Unit
Particle number	N	10,000	
Particle density	ρ	2600	kg/m ³
Particle radius	r	3, 4, 5	mm
Young's modulus	E	65	GPa
Poisson's ratio	ν	0.12	
Coefficient of restitution	e	0.95	
Time step	Δt	1.0e-7	s
Particle-particle sliding friction	μ	0.5	
Particle-wall sliding friction	μ	0.0	
Particle-wall rolling friction	μ_r	0.0	
Rolling viscous damping	η_r	0.0	
Box length and height		1.0 and 0.6	m

the particles that are selected to calculate the macroscale stress in the direct shear box are initially located within region B, as shown in Fig. 2. The extraction of the central region of the whole granular assembly can also effectively minimize the boundary effects.

4 Investigation of macroscopic results

A series of numerical simulations were conducted with a variety of rolling friction coefficients μ_r to explore its effect on the shear behavior. $q = (\sigma_1 - \sigma_2)/2$ is the deviatoric stress, and $p = (\sigma_1 + \sigma_2)/2$ is the mean stress. Xiao et al. [46, 47] adopted the laboratory tests to verify the usual critical-state behavior of rockfill materials with complex shape. Zhao and Guo [48] confirmed that a complete description of the critical state of a granular material must consider a critical fabric structure relevant to the critical stress. They further put forth that the definition of the critical state involves three criteria, namely, $\eta = \eta_c (\eta = q/p)$, $e = e_c$ (void ratio), and $K = K_c$. Figure 3a adequately describes the linear behavior between η_c and e_c with an increase in the rolling friction coefficient. K is the joint invariant of the deviatoric stress tensor s_{ij} ($s_{ij} = \sigma_{ij} - 1/3\delta_{ij}$) and the deviatoric fabric tensor F'_{ij} ($F'_{ij} = F_{ij} - 1/3\delta_{ij}$), which is expressed as:

$$K = s_{ij}F'_{ij} \tag{21}$$

K_c can behave as an effective indicator of the compatibility of the stress condition with fabric structures at critical state [48]. The rolling friction strongly affects the microscopic fabric, which makes it necessary to explore the dependence of the critical-state anisotropy variable K_c on the rolling friction coefficient. As seen in Fig. 3b, K_c evidently increases as the rolling resistance is increased, which exhibits a linear relationship between K_c and μ_r . This observation indicates that the validity of utilizing the term K_c to serve as the critical-state index should be evaluated rationally in accordance with the rolling friction.

In terms of the relationship between the microscale properties and macroscopic responses, the coaxiality between the fabric and external stress should be explored. As shown in Fig. 4a, it is interesting to note that a linear correlation between the principal stress direction θ_σ and θ_c is evident, which demonstrates that the coaxiality between the fabric and stress is strictly confirmed within various conditions of rolling friction during all the loading stages. To combine the anisotropic factors with the macroscopic response, we calculate the stress ratio q/p by means of Eq. (20). Hence, the stress ratio can be expressed by the fabric and force. The comparison between the external stress ratio [calculated

Fig. 3 Critical-state indexes within various conditions of rolling resistance: **a** η_c and e_c under different rolling frictions; **b** The relationship between the critical-state anisotropy variable K_c and the rolling friction coefficient

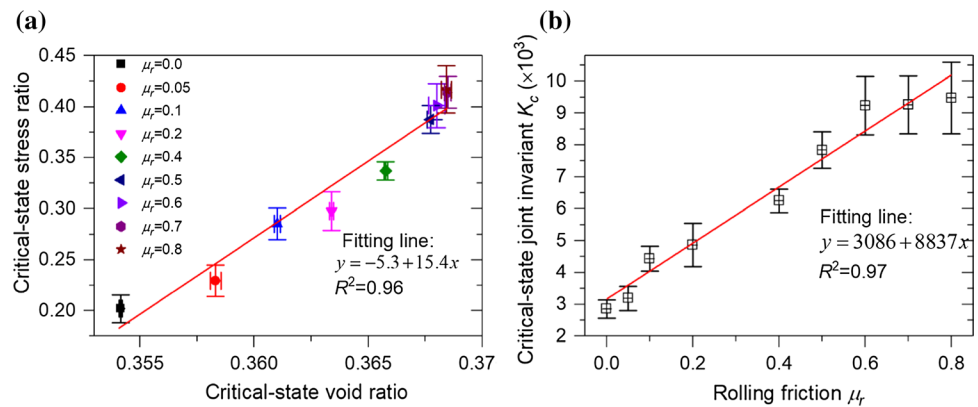
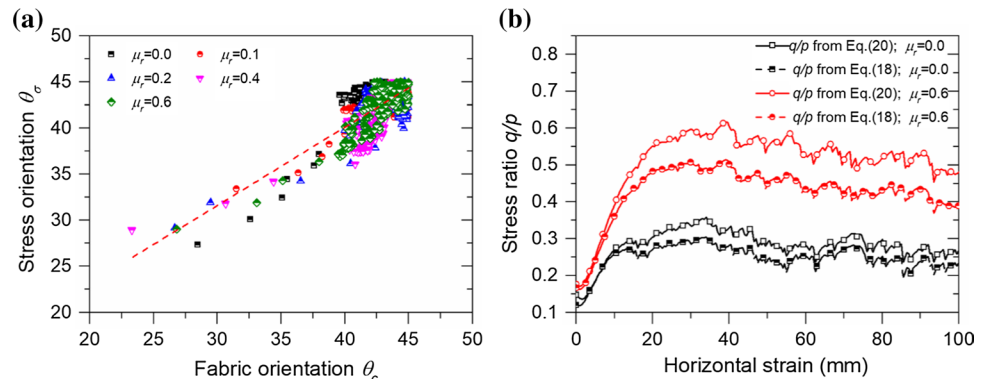


Fig. 4 Macro- and micro-scale relationship for different conditions of antirotation: **a** the relationship between the stress orientation and fabric orientation; **b** the comparison between the external stress ratio and the stress ratio calculated by stress-force-fabric relationship



from Eq. (18)] and the stress ratio calculated by Eq. (20) is presented in Fig. 4b. The comparison shows that the coincidence between the external stress ratio and the fabric-force-based stress ratio by Eq. (20) is well fulfilled when μ_r is low. When μ_r increases (when $\mu_r = 0.6$), the stress ratio q/p obtained from the stress tensor given in Eq. (20) is slightly larger than the stress ratio from the external stress tensor calculated from Eq. (18), which also gets discovered by Rothenburg and Bathurst [33].

5 Microscopic characteristics

The DEM provides an in-depth perspective for extracting the particle-scale information, thus embodying the strategy of probing into the fundamental mechanism of microscopic behavior. The local structural mechanism of sustaining the capacity and the contact force features are pivotal and underlying aspects of granular assemblies, in which the different mechanisms of rolling resistance can be explained.

5.1 Contact force transmissions and local structures

In discrete granular assembly, the external stress can be decentralized to unique contact networks, which generate the force transmission chains, shown in Fig. 5. The data are extracted from the critical-state particles, which are originally located in region B described in Fig. 2a, and the position is characterized by the X-axis and Y-axis. Owing

to the conditions that the shear band is limited to a region that contains 5–10 particles [49], it is evident that the force chain distributions exhibit the most distinctive characteristics within the shear band region for samples with different rolling resistances. Although the networks of force chains become fewer and scattered when the rolling resistance is increased, the magnitudes of the contact forces, displayed by the thickness and color of columns in Fig. 5, are elevated. Based on the enlarged local voids (marked by red circles in Fig. 5c) between force chains, it is demonstrated that more contacts begin to lose the opportunity to sustain forces with an increasing rolling friction coefficient. As illustrated from the spatial distribution of the coordination number in Fig. 5d, it is clear that the region at or near the shear band has the largest proportion of nonmechanical particles (with zero or only one contact) which are depicted by the color red. As noted by Thornton [50], these particles do not sustain the force transmission. Hence, it can be concluded that the increase in the rolling resistance can make the force chains sparse, thus creating more floating particles, especially within the shear band.

Figure 6 demonstrates the particle structural mechanisms of increasing the rolling resistance, which is analogous to the description of Iwashita and Oda [4]. The column-like structure of Fig. 6a, characterizing the local structure in the absence of the rolling friction, contrasts with that shown in Fig. 6b, which shows a bent structure with the exertion of rolling torques on the contacts and generates the arching mechanism. As evidently shown in Fig. 5c, the increased

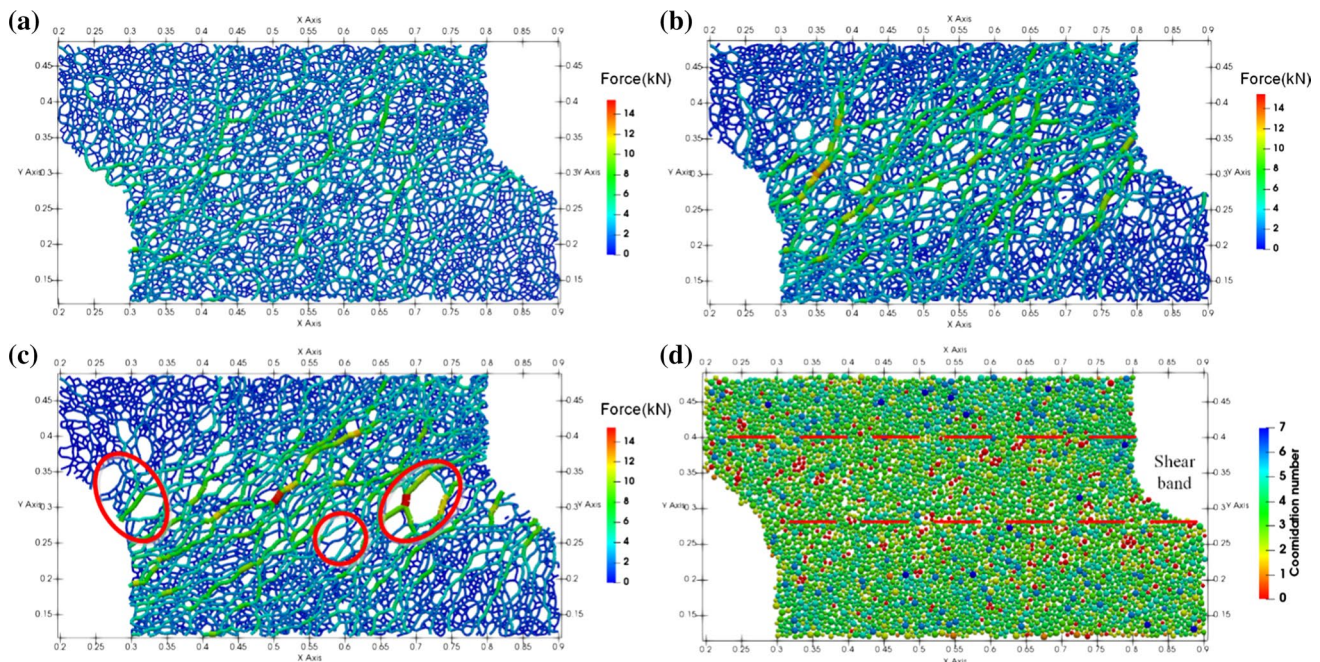


Fig. 5 Force chains and coordination number descriptions under different influences of rolling resistance: **a** when $\mu_r = 0.0$; **b** when $\mu_r = 0.2$; **c** when $\mu_r = 0.6$; **d** The spatial distribution of the coordination number (when $\mu_r = 0.2$)

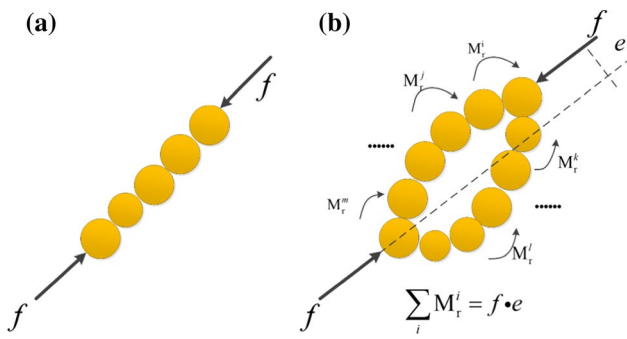


Fig. 6 Particle structural features under different rolling friction conditions: **a** without rolling resistance; **b** With rolling resistance

void space between the force chains can illustrate the mechanisms shown in Fig. 6b, which indicates that more particles that have begun to lose the capacity of sustaining forces are caged by the skeleton constituted by the arching particles. The elevated void ratio discussed in Fig. 3a can also verify the increased local void within the force chains in Fig. 6b when μ_r increases. Due to the sparsification of the force network, the particles that mainly function as the load-carrying structures tend to sustain more intense forces with an improvement in the rolling friction.

The strengthened local arching structures can also be explained from the effects of the rolling resistance on the mobilization friction. Owing to the fact that the sliding contacts are critical to the analysis of plastic deformation [51], the frictional saturation index $\xi = f_t / \mu f_n$ is adopted to characterize the effects of rolling friction on the sliding phenomenon within contacts. The contacts with $f_t < \mu f_n$ are donated as elastic contacts, and $f_t = \mu f_n$ represents the yield criterion and corresponds to plastic contacts [52]. As shown in Fig. 7a, the probability distributions of frictional saturation $P(\xi)$ nearly exhibit linear curves within various rolling friction conditions at the critical state. $P(\xi)$ gradually decreases with an increase in ξ , and an improvement in the rolling friction can make the contacts more prone to being plastic because of the increased $P(\xi)$ at larger values of ξ . The $P(\xi)$ values when

ξ approaches 1.0 are shown in the insert of Fig. 7a, which indicates that $P(\xi)$ first increases with an increase in μ_r , and then experiences a slight decrease at larger μ_r conditions. Hence, it is evident that the increase in the rolling friction can elevate the plastic magnitudes to some extent when μ_r is less than 0.6. To evaluate the overall level of friction mobilization, the mean friction mobilization index is employed:

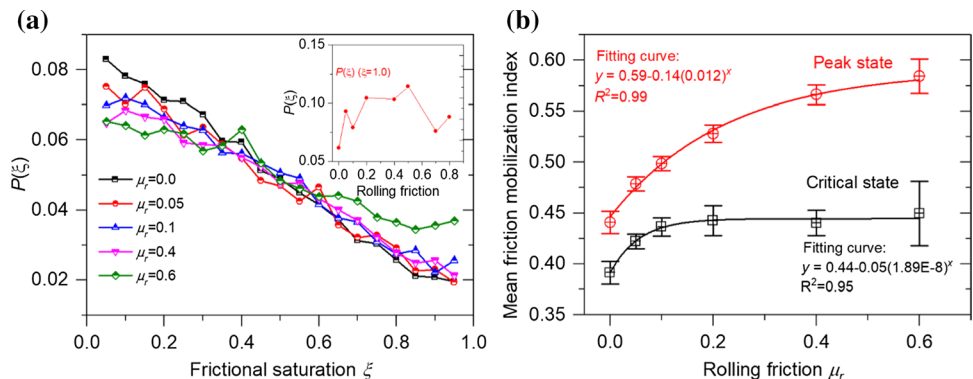
$$\bar{I}_m = \frac{1}{N} \sum_{c \in N} \frac{f_c^t}{\mu f_n^c} \tag{22}$$

In Fig. 7b, we observe that the distinctions between the peak \bar{I}_m values of various rolling conditions are evidently larger than those of the critical-state values. The critical-state \bar{I}_m values are nearly the same when μ_r exceeds 0.1 in comparison to the gradually increasing trend of peak \bar{I}_m values with an increase in μ_r . It can be concluded that the anti-rotation can evidently influence the sliding behavior within the contact system, especially during the peak state. However, the effects of the rolling resistance on the sliding mobilization nearly disappear during the critical-state period.

5.2 Strong-network force chains

As previously mentioned, the coexisting force chain networks, namely, the strong and weak networks as defined by Radjai et al. [53], play different mechanical roles in the sample. The forces that exceed the average contact force \bar{f} belong to the strong network, and the weak network includes forces lower than \bar{f} . The strong network occupies the dominant force magnitude when sustaining the deviatoric load, and the weak network with a relatively lower force magnitude performs the function of supporting the strong force chains. According to the force chain networks in Fig. 5, the magnitude of the strong force chain tends to increase when μ_r increases, but its proportion in the whole force network weakens, especially at larger μ_r conditions. For tests with a larger rolling friction shown in Fig. 5, some of the weak force chains supporting the strong network are weakened and even vanish, thus giving rise to a greater burden of certain

Fig. 7 **a** Probability distributions $P(\xi)$ of the frictional saturation index for elastic contacts ($f_t < \mu f_n$) under various conditions of rolling resistance; **b** the mean friction mobilization index for different rolling influences at the critical state



local particles with strong forces. As shown in Fig. 8(a), the proportion of the strong contacts gradually decreases towards steady values as the rolling friction increases. The decrease in the strong contact ratio can indicate the increased localization of strong force chains when the rolling resistance increases.

Considering the dominant role of strong force chains, the orientation order parameter is analyzed to characterize the orientation of the strong force chains [54]:

$$S_{orient} = \frac{1}{\sum_i l_i^2} \sum_i l_i^2 \cos^2 \theta_i - 1 \tag{23}$$

where l_i represents length of the branch vector, and θ_i is the angle between the contact force and the vertical direction. When $S_{orient} = 1.0$, all the strong contact forces are vertically distributed. When $S_{orient} = 0.0$, the forces are oriented at 45° or directed randomly, and $S_{orient} = -1.0$ indicates a horizontal orientation of the strong contact forces. As shown in Fig. 8b, the orientation order parameter linearly decreases with an increase in μ_r , which indicates that the strong forces first tend to be more horizontally oriented with an increase in the rolling resistance. At the critical and peak states, the relationship between the orientation order parameter and rolling friction is different.

Peters et al. [55] has identified that the stronger forces are carried by certain chainlike particles groups that are regarded as the force chains. The magnitude and the orientation of force chains depend on the particle stress tensor:

$$\sigma_{ij}^{particle} = \frac{1}{V_p} \sum_{c=1}^{N^c} f_i^c r_j^c, \tag{24}$$

where the terms V_p and N^c represent the particle volume and the coordination number respectively. The force chains are quasi-linear, and can reflect the authentic trajectory of the principal stress with most compression [56, 57]. The minor principal stress is the most compressive principal stress. As put forward by Campbell [58], the minimum particle number that constitute a force chain is three. To be brief, the adequate algorithm adopted to extract the force chains can

refer to the work of Peters et al. [55]. In Fig. 9, we present the force chain structures under various conditions of rolling friction. It demonstrates that the force chains within the condition of no rolling resistance are scattered in contrast to the concentrated clumps of force chains with increasing rolling friction. On the other hand, the structures exhibit more orientation towards the maximum principal stress direction when μ_r increases. Especially for $\mu_r = 0.6$, almost all the force chains are directional.

The adequate information of force chains gets explained in Fig. 10. The length of force chains is defined by the number of particles within a force chain. An exponential relationship between the force chain length and the number of force chains is verified. With increasing rolling resistance, the proportion of lower-length force chains decreases and that of the larger-length force chains get increased. The total number of force chains gets reduced when μ_r increases from 0.0 to 0.5, and then experience a slight increase trend. By comparison, the characteristics of the average length of force chains exhibit an inverse trend. It indicates that when μ_r exceeds 0.6 the increase of the rolling coefficient cannot strengthen the constitution of force chains. Hence the utilization of rolling coefficient to characterize the effects of rolling resistance should be limited by a reasonable scope, and this scope of μ_r in our present work is 0.5.

5.3 Force distributions and orientation

Owing to the fact that the characteristics of force chains intimately relate to the force distribution [59], a qualitative characterization of the force transmission behavior is significant. The probability density function (PDF) of the normal contact force is plotted in Fig. 11 (log–log), where the data are adopted from the critical state. As the bimodal character is usually observed in the interparticle force distribution within granular assemblies, an exponential decrease for the forces above the average force \bar{f}_n and a power-law distribution for the forces below \bar{f}_n are exhibited [53, 60, 61]:

$$P(f_n/\bar{f}_n) \propto \begin{cases} (f_n/\bar{f}_n)^{-\beta}, & f_n < \bar{f}_n \\ e^{\alpha[1-f_n/\bar{f}_n]}, & f_n > \bar{f}_n \end{cases} \tag{25}$$

Fig. 8 Critical-state strong networks within different conditions of rolling frictions: **a** the proportion of strong contacts; **b** the orientation order parameter for strong networks

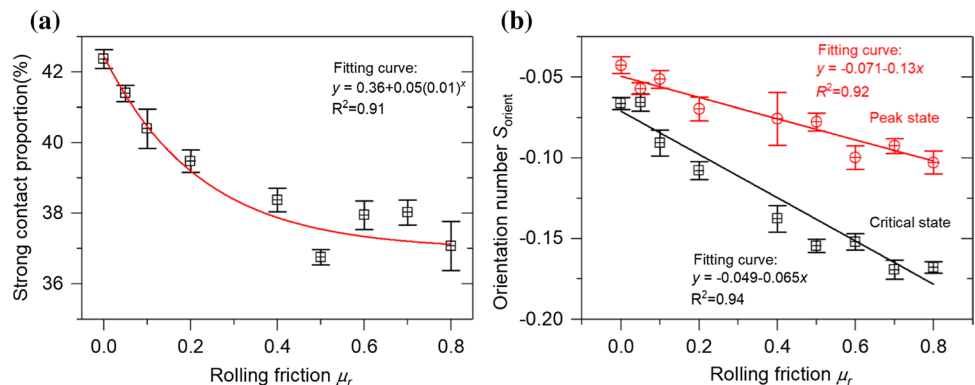
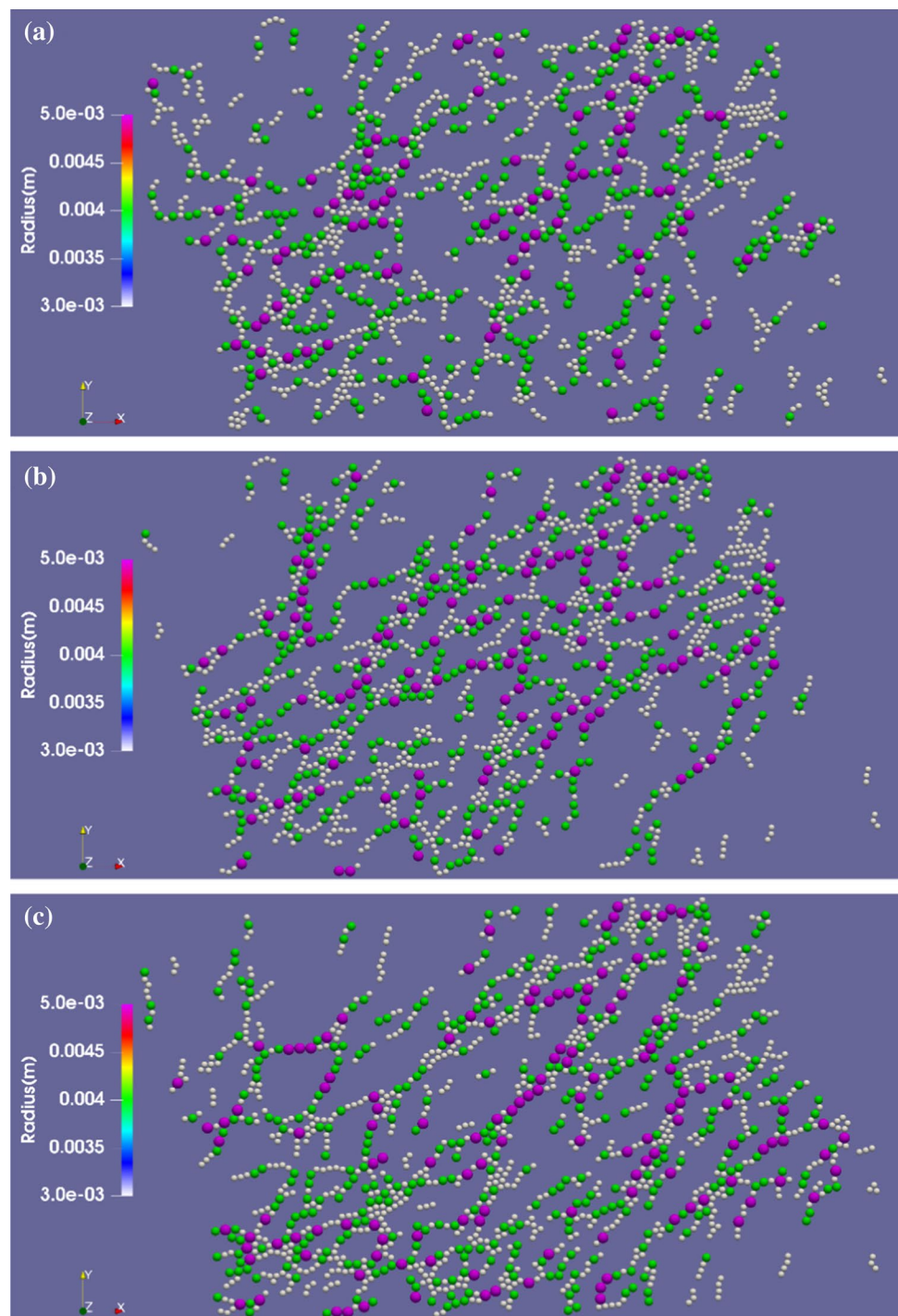


Fig. 9 Force chain structures extracted from the granular assemblies within different conditions of rolling friction: **a** when $\mu_r = 0.0$; **b** when $\mu_r = 0.2$; **c** when $\mu_r = 0.6$



This result indicates that the distribution of normal contact forces becomes wider in the sample as the rolling resistance increases. The coefficient α increases towards a steady value with an increase in μ_r , which is in contrast to the descending trend of β .

It has previously been verified that $P(f_n/\bar{f}_n)$ occupies a small peak or a plateau at small f_n values and has an exponential tail when f_n is large [62, 63]. As shown in

Fig. 11, a small peak exists when f_n/\bar{f}_n equals 1.0 for the tests with $\mu_r < 0.05$. With an increase in μ_r , the peak phenomenon gradually disappears. Owing to the conclusion that the emergence of the peak represents the jamming characteristics [63], the reduction in rolling resistance can effectively strengthen the jamming state. The observation can also be explained from the conclusion of O'Hern et al.

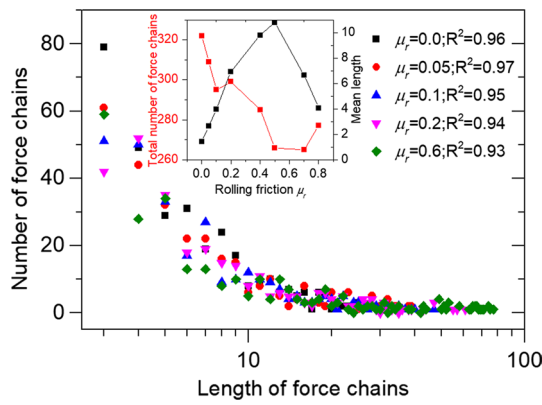


Fig. 10 Distributions of the number of force chains with respect to the length of force chains under different rolling condition

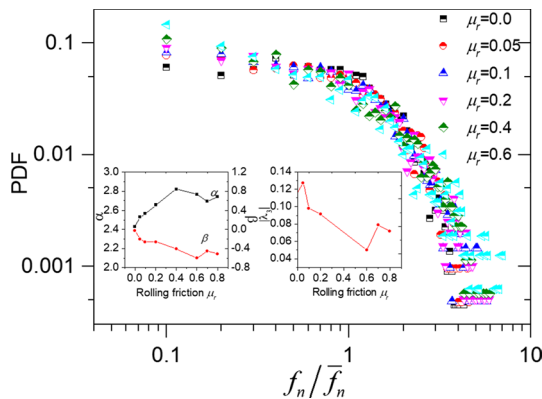


Fig. 11 Probability distribution functions of normal contact forces at the critical state within various conditions of rolling frictions

[62] that the increase in the solid fraction can induce the peaks near $f_n/\bar{f}_n = 1.0$, and the decrease in μ_r corresponds to the larger solid fraction in our work. The increased density of force chains in Fig. 5a can also verify the increased magnitude of jamming when μ_r is reduced.

The exponential tails when $f_n > \bar{f}_n$, as shown in Fig. 11, fall off more slowly when μ_r increases. When the stress among the granular assemblies is elevated, the exponential tail can experience a gradual transition to a Gaussian force distribution, and the transition is derived from the force chain development [62]. To characterize the deviation from the exponential feature when $f_n > \bar{f}_n$, the exponent of the quadratic function [63], $P(f_n/\bar{f}_n) \propto e^{[\lambda_1 - \lambda_2 f_n/\bar{f}_n + \lambda_3 (f_n/\bar{f}_n)^2]}$, is adopted. The absolute value of $|\lambda_3|$ can be responsible for the transformation between the exponential and Gaussian distributions, which are depicted in the insert Fig. 11. It is observed that $|\lambda_3|$ gradually decreases towards a steady level when the rolling friction increases, which indicates that the improvement of rolling resistance can make $P(f_n/\bar{f}_n)$ prone to an exponential attribution at larger values of f_n/\bar{f}_n . In

other words, a reduction in the rolling friction can induce $P(f_n/\bar{f}_n)$ to approach a Gaussian distribution, which violates the usual robust exponential form of granular packing [64]. Hence, the utilization of the rolling friction in a numerical simulation is reasonable.

The stress fluctuations can be attributed to the variation of force chains, and a localization of force chains gradually emerges from the loading process [65]. The localization originates from the disorder within the particle arrangement. The participation number ζ is used to quantify the degree of localization [61]:

$$\zeta = \left(N \sum_{i=1}^N q_i^2 \right)^{-1}, \quad q_i = \frac{f_i}{\sum_{k=1}^N f_k} \tag{26}$$

where N represents the entire contact number within the granular assemblies, and f_i is the force magnitude at each contact point. The characterization of force chains is demonstrated in Fig. 12. As shown in Fig. 12a, the participation number decreases with an increase in the rolling resistance, which exhibits a linear relationship with μ_r . This observation indicates that the force chains are more localized with an increase in μ_r . In terms of the heterogeneity of the force chain magnitude, the *Gini* coefficient is employed to characterize the distributions of the force magnitude [66]:

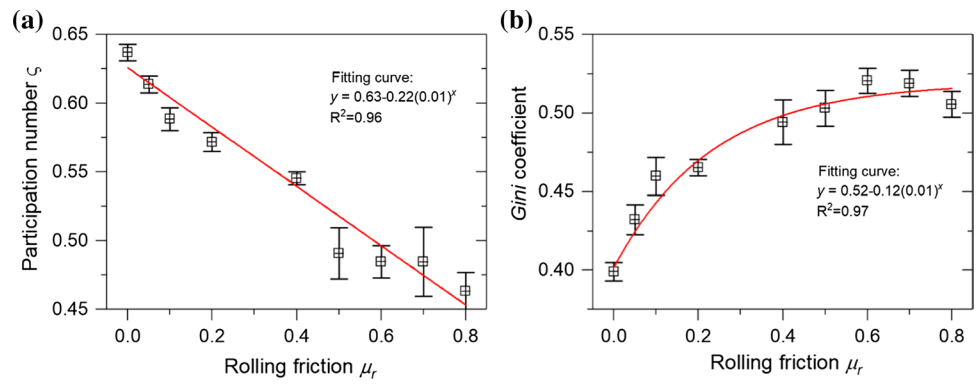
$$Gini = \frac{1}{N_c} \left(N_c + 1 - 2 \left(\frac{\sum_{i=1}^{N_c} (N_c + 1 - i) f_i^n}{\sum_{i=1}^{N_c} f_i^n} \right) \right) \tag{27}$$

The term N_c is denoted as the number of contacts. The increase of *Gini* coefficient indicates more evident inhomogeneity among the whole contact system. The *Gini* coefficient is usually adopted to characterize a nation’s income inequality and represent the homogeneity of certain quantities [66]. The normal contact force f_i^n is sorted in a nondecreasing order ($f_i^n \leq f_{i+1}^n$). The *Gini* coefficient is calculated from the critical-state data. *Gini* = 0.0 implies total homogeneity of the normal contact forces, in contrast to total heterogeneity when *Gini* equals 1.0. Figure 12(b) indicates that the force heterogeneity is intensified when the rotational resistance is elevated and tends to be constant when μ_r exceeds 0.6. Therefore, it can be concluded that the samples with less rolling friction behave more homogeneously from both the geometrical features and magnitude distribution of force chains.

5.4 Local strain and nonaffine displacements

For crystals, translational invariant particles will undergo the same number of local deformation under the uniform stress. On the contrary, the local deformation of amorphous materials changes strongly due to the change of particle environment.

Fig. 12 Characterizations of force chains at the critical state: **a** the participation number describing the localization of force chains with different rolling resistances; **b** the Gini coefficients with different rolling frictions



Therefore, the displacement of particles can no longer be described by a single affine transformation. The notion of non-affine can be utilized to characterize the deviation from the affine deformation field. For the amorphous granular materials, the local strain is heterogeneous, and the nonaffine displacement of particles is evident among granular assemblies [67]. The behaviors of neighbor particles also differ from each other within different regions of granular materials. Hence the local strain and nonaffinity are necessary to be adopted to explore the strain localization and spatial distribution of local properties. Many previous work also confirmed that the nonaffine measures can be an effective indicator to describe the characteristics of strain localization [68–70].

The affine tensor Γ utilizes the displacement of neighbor particles to obtain the affine displacement field. The mean-square difference of the relative displacements between nearest-neighbor particles and the central reference particle determines the affine tensor Γ . The mean-square difference is expressed as [71]:

$$D^2 = \sum_n \sum_i \left(r_n^i(t) - r_0^i(t) - \sum_j (\delta_{ij} + \Gamma_{ij})(r_n^j(t - \delta t) - r_0^j(t - \delta t)) \right)^2 \tag{28}$$

where n is number of neighbor particles for the reference particle. During the traversal of neighbor particles, the region is defined as the area of the circle with the radius of $1.5d_{\max}$, and d_{\max} represents the maximum diameter of the particle assembly. The terms i and j represent the adequate coordinate system. $r_n^i(t)$ is the i th component of the spatial position for the n th neighbor particle at time t . By minimizing D^2 , the affine tensor Γ can be calculated [67]:

$$\Gamma = \sum_k X_{ik} Y_{kj}^{-1} - \delta_{ij} \tag{29}$$

$$X_{ij} = (r_n^i(t) - r_0^i(t))(r_n^j(t - \delta t) - r_0^j(t - \delta t)) \tag{30}$$

$$Y_{ij} = (r_n^i(t - \delta t) - r_0^i(t - \delta t))(r_n^j(t - \delta t) - r_0^j(t - \delta t)) \tag{31}$$

Based on the affine tensor, the local strain ϵ^L can be deduced [72]:

$$\epsilon^L = \frac{-(\Gamma + \Gamma^T)}{2} \tag{32}$$

Hence the local deviatoric strain ϵ_q^L can be calculated:

$$\epsilon_q^L = \sqrt{\frac{2}{3} \epsilon_{dev}^L : \epsilon_{dev}^L} \tag{33}$$

In our work, the time interval δt is 0.01 s and the calculation of both the local strain and nonaffine deformation is performed at critical state. In Fig. 13, the distributions of local deviatoric strains ϵ_q^L are exhibited. It demonstrates that the distributions of the local deviatoric strain show little differences for various conditions of rolling resistance. For ϵ_q^L with less magnitude, the increase of rolling friction can slightly increase the corresponding proportion. At large level of ϵ_q^L , the distributions within various μ_r conditions are almost the same. It indicates that the local deviatoric strain seems not to be influenced by the change of the rolling friction, especially within the larger magnitude of ϵ_q^L .

Based on classical mechanics and dynamics theory, Goldenberg et al. [73] proposed displacement fluctuation

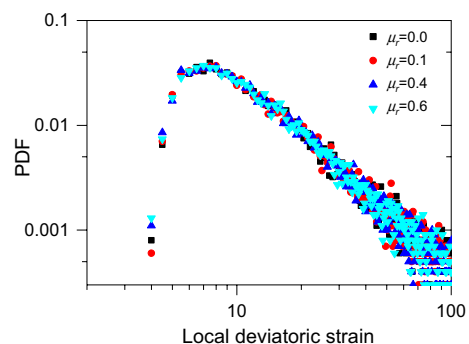


Fig. 13 Probability distribution of the local deviatoric strain within different conditions of rolling resistance

under non-affine deformation. On the basis of Goldenberg et al. [73], Chikkadi and Schall [74] defined a continuous displacement field based on the weighted method of coarse-graining function. The fluctuation part can be obtained by subtracting the displacement of a single particle from the continuous displacement field, which is considered as the local measurement of non-affine deformation. The continuous displacement field with coarse-graining function is defined as:

$$U(\mathbf{r}, t, \delta t) = \frac{1}{N} \sum_{j=1}^N \Delta \mathbf{r}_{ij}(t, \delta t) \Phi(\mathbf{r}_{ij}(t - \delta t) - \mathbf{r}) \tag{34}$$

and the nonaffine displacement is:

$$\Delta \mathbf{r}'_i(t, \delta t) = \Delta \mathbf{r}_i(t, \delta t) - U(\mathbf{r}, t, \delta t) \tag{35}$$

where the term N represent the total particle number. $\Delta \mathbf{r}_{ij}$ represents the difference of displacement vectors between the central reference particle and its peripheral particles. Φ is the coarse-graining function:

$$\Phi(\mathbf{r}) = H(R^2 - d_0^2) \tag{36}$$

In this paper, the term d_0 equals to $1.5d_{\max}$.

The probability distribution of local nonaffine deformation is described in Fig. 14 under different conditions of rolling friction. Unlike the local deviatoric strain, the distribution of the nonaffine displacement behave differently among different value domains. When $\Delta r'_i$ is below $1E-6$, the particles with more rolling resistance account for more proportions. When the value of nonaffine displacement increases, the increase of μ_r evidently reduces the particle percentage. The nonaffine displacement can also characterize the plasticity [72]. According to Fig. 14, for all conditions of μ_r , the particles with low-magnitude plasticity take the most proportions. It can also be concluded that the decrease of rolling resistance can intensify the plasticity. Namely, for high-level nonaffine displacements, more particles tend to be plastic when μ_r decreases.

Figure 15 shows the distribution of the particle nonaffine deformation within the whole sample region. The half height of the sample is the boundary of the upper and lower half boxes, and this region corresponds to the shear concentration domain. Within the shear concentration region, high value of nonaffinity is observed. When the distance from the concentration domain gets increased, the nonaffine displacement obviously get reduced. It illustrates that the plasticity behavior is more prominent in shear concentration region, and the area where the plasticity carriers concentrate is also known as the shear transformation zone (STZ) [72, 75]. Therefore it is evident that the shear transformation zones are mainly localized among the shear boundary of the two half boxes.

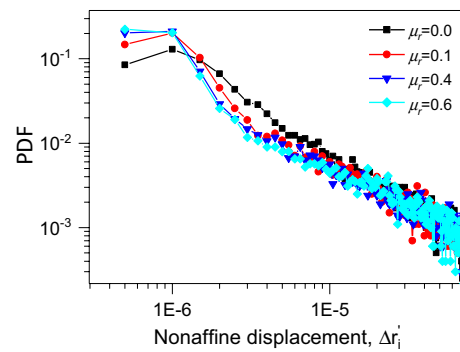


Fig. 14 Probability distributions of nonaffine displacement for different rolling conditions

To characterize the magnitude of localization of nonaffine displacements, the participation ratio $p_{\Delta r'}$ can be adopted [67]:

$$p_{\Delta r'} = \frac{(\sum_i \Delta r'_i \Delta r'_i)^2}{N \sum_i (\Delta r'_i \Delta r'_i)^2} \tag{37}$$

The term N represents the particle number, and $\Delta r'_i$ is donated as the nonaffine displacement of particle i . When the sample deformation refer to all the particles, the participation ratio approaches the order unity with less magnitude of localization. Figure 16 shows the change of the participation ratio with respect to the rolling friction coefficient. The improvement of rolling resistance can make the participation ratio gradually increases. It indicates that the nonaffine displacements are more localized within the samples with less rolling friction. Considering the fact that the nonaffine deformation within granular assemblies depend on the particle arrangements, the increase of rolling resistance can make the particles more difficult to freely move around. From Fig. 14, it also clearly exhibits the more proportion of high-magnitude nonaffinity for the samples with less rolling resistance. Hence the high-level nonaffine displacements with less rolling friction correspond to the more evident localization.

5.5 Anisotropic characteristics

As discussed previously in Sect. 2, the stress tensor can be quantitatively expressed as a function of the anisotropy parameters. A comprehensive study on different anisotropy sources is presented below.

We present the distribution of the directional contact proportions, mean normal contact forces, and mean contact tangential forces in the polar diagrams (Fig. 17), where the values of $\mu_r = 0.0$, $\mu_r = 0.2$, and $\mu_r = 0.6$ are chosen to be the analytical perspectives. To make our analysis brief, the distributions in Fig. 17 only refer to the

Fig. 15 Spatial distribution of nonaffine displacements ($\mu_r = 0.4$)

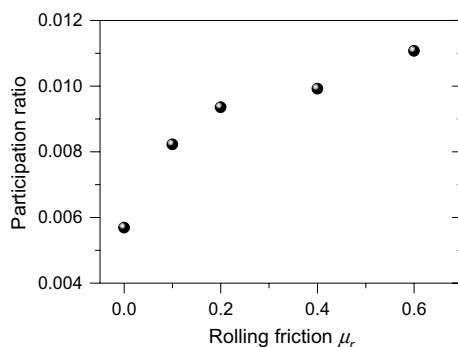
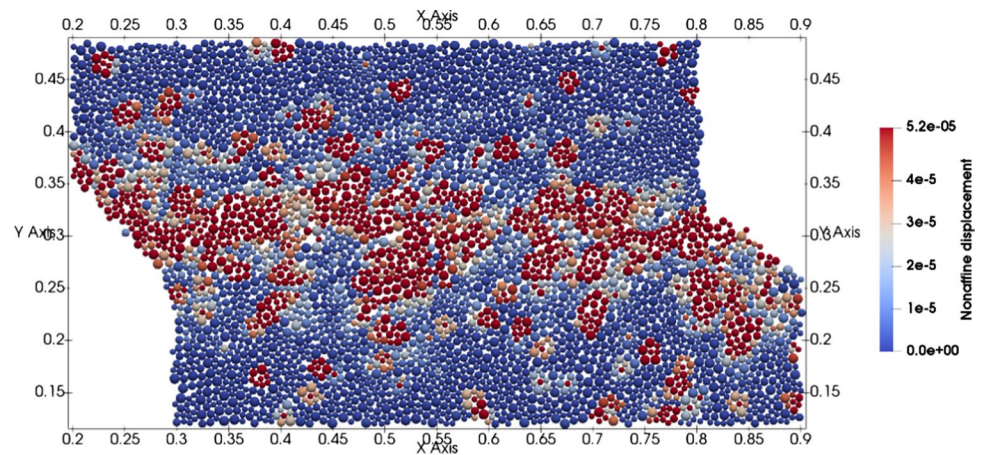


Fig. 16 The relationship between the rolling friction and the participation number

critical state. Both the distributions of the contact proportions and mean normal contact forces become more anisotropic when μ_r increases. For contact tangential forces, with an increased μ_r , the distribution tends to be more butterfly-shaped, and the magnitude of the mean tangential contact forces located along the principal stress direction gradually decreases.

The anisotropy parameters related to the normal contact, and normal contact and tangential force distributions are exhibited in Fig. 18. It is evident that the rotational resistance can enhance the values of the anisotropy parameters, which indicates a linear relationship between all the parameters and the rolling friction coefficient. Although the increasing trend is not evident when μ_r exceeds 0.6 for the contact normal anisotropy, the overall monotonic increasing trend still exist. The slopes of the fitting lines for various anisotropy parameters are nearly the same at the critical state.

6 Conclusion

In this paper, by means of the DEM with a Hertz-Mindlin model considering rolling friction, numerous direct shear tests are performed with various conditions of rolling friction. The mechanical and geometrical roles of the rolling friction are reflected in structural characteristics, force transmission, and many fundamental microscale responses. The main conclusions from the observation are given below:

1. The coaxiality between the fabric and stress tensors is fulfilled within various conditions of rolling friction, and the stress-force-fabric relationship is well verified using different rolling friction coefficients during the shearing process. The critical-state stress ratio and void ratio are linearly correlated for various conditions of rolling resistance. The critical-state anisotropy variable also gets linear increase with respect to the rolling friction coefficient.
2. The force chain networks become sparse with an improvement in the rolling resistance, and the localization of force chains quantitatively depends on the rolling resistance. The number of force chains decreases exponentially with the increase of force chain length. The decrease of rolling friction coefficient can accelerate the exponential decay rate. The local structural mechanisms related to the rotational resistance are evidently recognized by the local buckling phenomenon of particles, which corresponds to the discrete distribution of force chain networks in space. The distribution of contact force magnitudes exhibits evident inhomogeneity with the increase of rolling resistance. Both the peak and critical values of the mean friction mobilization index increase with an increase in μ_r . The exponential tail of the probability distribution of normal contact forces experiences a transition towards a Gaussian distribution when the rolling friction decreases.

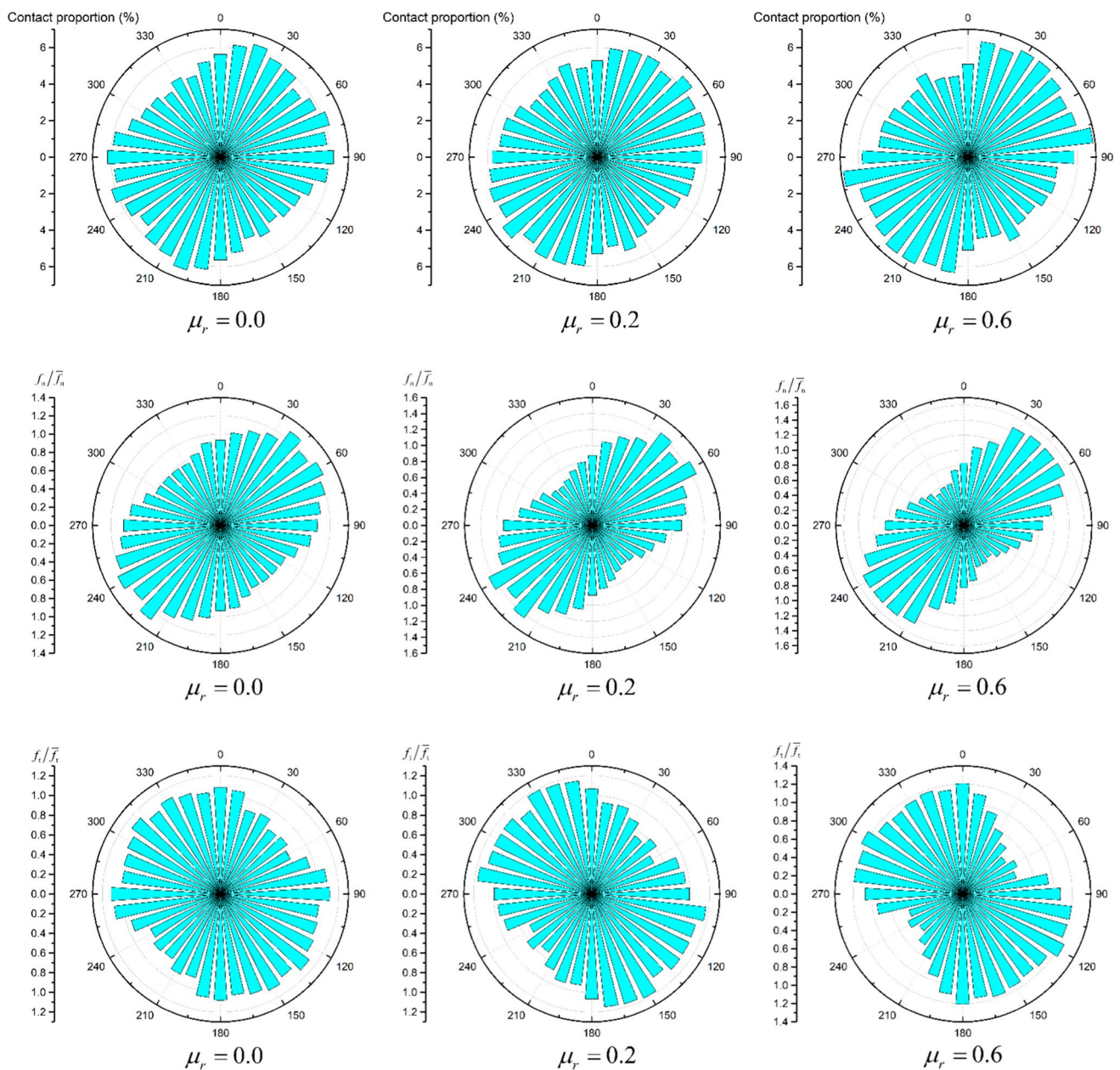


Fig. 17 Polar diagrams of the directional contact proportion, mean normal contact force and mean contact tangential force under the influences of three types of rolling frictions

3. The local deviatoric strains among various rolling conditions nearly occupy the same characteristics of distribution at larger values. The proportion of particles with lower nonaffine displacements gradually gets increased when the rolling resistance increases in contrast to the descending trend for larger nonaffine displacements. For samples with relatively lower rolling friction, the particles tend to become more plastic. The shear transformation zone is mainly located at the shear concentration zone where the boundary of the upper and lower half boxes locates.
4. The improvement of the rolling friction clearly strengthens the arching effect between particles and the capability of a strong network to sustain the deviatoric load. Concomitantly, the role of the weak network in supporting the strong force chain is weakened or locally eliminated. Along with the increased prominence of the rolling resistance, less strong contacts are generated. Both the distributions of the normal contact and normal contact forces become more anisotropic when μ_r increases. The critical-state anisotropy parameters are all linearly correlated to the rolling friction coefficient.

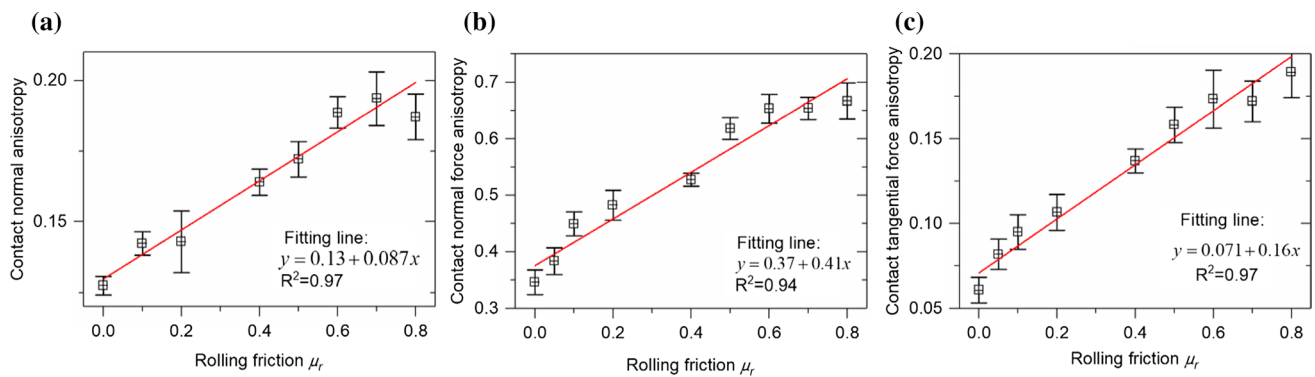


Fig. 18 The relationship between the anisotropy parameters and the rolling friction coefficient

Acknowledgments This work was financially supported by the National Key R&D Program of China (Grant No. 2017YFC0404801), the National Natural Science Foundation of China (Grant No. 51579193), the Fundamental Research Funds for the Central Universities (Grant No. 2042017kf0277), and The Major Special Project of Guizhou Province (Grant No. (2017)6013-2).

Compliance with ethical standards

Conflict of interest The all authors declare that no conflict of interest exists in the submission of this manuscript and that it is compliant with ethical standards.

References

- Ai, J., Chen, J.F., Rotter, J.M., Ooi, J.Y.: Assessment of rolling resistance models in discrete element simulations. *Powder Technol.* **206**, 269–282 (2011). <https://doi.org/10.1016/j.powtec.2010.09.030>
- Iwashita, K., Oda, M.: Rolling resistance at contacts in simulation of shear band development by DEM. *J. Eng. Mech.* **124**, 285–292 (1998). [https://doi.org/10.1061/\(ASCE\)0733-9399\(1998\)124:3\(285\)](https://doi.org/10.1061/(ASCE)0733-9399(1998)124:3(285))
- Oda, M., Iwashita, K.: Study on couple stress and shear band development in granular media based on numerical simulation analyses. *Int. J. Eng. Sci.* **38**, 1713–1740 (2000). [https://doi.org/10.1016/S0020-7225\(99\)00132-9](https://doi.org/10.1016/S0020-7225(99)00132-9)
- Iwashita, K., Oda, M.: Micro-deformation mechanism of shear banding process based on modified distinct element method. *Powder Technol.* **109**, 192–205 (2000). [https://doi.org/10.1016/S0032-5910\(99\)00236-3](https://doi.org/10.1016/S0032-5910(99)00236-3)
- Tordesillas, A., Walsh, D.C.S.: Incorporating rolling resistance and contact anisotropy in micromechanical models of granular media. *Powder Technol.* **124**, 106–111 (2002). [https://doi.org/10.1016/S0032-5910\(01\)00490-9](https://doi.org/10.1016/S0032-5910(01)00490-9)
- Jiang, M.J.J., Yu, H.-S., Harris, D.: A novel discrete model for granular material incorporating rolling resistance. *Comput. Geotech.* **32**, 340–357 (2005). <https://doi.org/10.1016/j.compgeo.2005.05.001>
- Estrada, N., Taboada, A., Radjai, F.: Shear strength and force transmission in granular media with rolling resistance. *Phys. Rev. E* **78**, 1–11 (2008). <https://doi.org/10.1103/PhysRevE.78.021301>
- Oda, M., Kazama, H., Konishi, J.: Effects of induced anisotropy on the development of shear bands in granular materials. *Mech. Mater.* **28**, 103–111 (1998). [https://doi.org/10.1016/S0167-6636\(97\)00018-5](https://doi.org/10.1016/S0167-6636(97)00018-5)
- Estrada, N., Azéma, E., Radjai, F., Taboada, A.: Identification of rolling resistance as a shape parameter in sheared granular media. *Phys. Rev. E Stat. Nonlinear Soft Matter Phys.* **84**, 10 (2011). <https://doi.org/10.1103/PhysRevE.84.011306>
- Mohamed, A., Gutierrez, M.: Comprehensive study of the effects of rolling resistance on the stress-strain and strain localization behavior of granular materials. *Granul. Matter* **12**, 527–541 (2010). <https://doi.org/10.1007/s10035-010-0211-x>
- Fukumoto, Y., Sakaguchi, H., Murakami, A.: The role of rolling friction in granular packing. *Granul. Matter* **15**, 175–182 (2013). <https://doi.org/10.1007/s10035-013-0398-8>
- Zhao, J., Guo, N.: Rotational resistance and shear-induced anisotropy in granular media. *Acta Mech. Solida Sin.* **27**, 1–14 (2014). [https://doi.org/10.1016/S0894-9166\(14\)60012-4](https://doi.org/10.1016/S0894-9166(14)60012-4)
- Taylor, D.: *Fundamentals of soil mechanics*. Limited.; New York, Chapman And Hall (1948)
- Saadat, A.S., Townsend, F.C.: State of the art: laboratory strength testing of soils. In: *Laboratory shear strength of soil*. ASTM International (1981)
- Terzaghi, K., Peck, R.B., Mesri, G.: *Soil mechanics in engineering practice*, 3rd edn, p. 664. Wiley, New York (1996)
- Potts, D.M., Dounias, G.T., Vaughan, P.R.: Finite element analysis of the direct shear box test. *Géotechnique* **37**, 11–23 (1987). <https://doi.org/10.1680/geot.1987.37.1.11>
- Ai, J., Langston, P.A., Yu, H.S.: Discrete element modelling of material non-coaxiality in simple shear flows. *Int. J. Numer. Anal. Methods Geomech.* **38**(6), 615–635 (2014)
- Dounias, G.T., Potts, D.M.: Numerical analysis of drained direct and simple shear tests. *J. Geotech. Eng.* **119**, 1870–1891 (1993). [https://doi.org/10.1061/\(ASCE\)0733-9410\(1993\)119:12\(1870\)](https://doi.org/10.1061/(ASCE)0733-9410(1993)119:12(1870))
- Masson, S., Martinez, J.: Micromechanical analysis of the shear behavior of a granular material. *J. Eng. Mech.* **127**, 1007–1016 (2001). [https://doi.org/10.1061/\(ASCE\)0733-9399\(2001\)127:10\(1007\)](https://doi.org/10.1061/(ASCE)0733-9399(2001)127:10(1007))
- Cui, L., O’Sullivan, C.: Exploring the macro- and micro-scale response of an idealised granular material in the direct shear apparatus. *Géotechnique* **56**, 455–468 (2006). <https://doi.org/10.1680/geot.56.7.455>
- Liu, S.H.: Simulating a direct shear box test by DEM. *Can. Geotech. J.* **43**(2), 155–168 (2006)
- Liu, C., Nagel, S.R., Schecter, D.A., et al.: Force fluctuations in bead packs. *Science* **269**(5223), 513–515 (1995)
- O’Hern, C.S., Langer, S.A., Liu, A.J., Nagel, S.R.: Random packings of frictionless particles. *Phys. Rev. Lett.* **88**, 4 (2002). <https://doi.org/10.1103/PhysRevLett.88.075507>

24. LIGGGHTS: a new open source discrete element simulation software. In: Proceedings of the fifth international conference on discrete element methods, London, UK (2010)
25. Oda, M.: The mechanism of fabric changes during compressional deformation of sand. *Soils Found.* **12**, 1–18 (1972). <https://doi.org/10.3208/sandf.47.887>
26. Oda, M.: Fabric tensor for discontinuous geological materials. *Soils Found.* **22**, 96–108 (1982). https://doi.org/10.3208/sandf.1972.22.4_96
27. Ken-Ichi, K.: Distribution of directional data and fabric tensors. *Int. J. Eng. Sci.* **22**, 149–164 (1984). [https://doi.org/10.1016/0020-7225\(84\)90090-9](https://doi.org/10.1016/0020-7225(84)90090-9)
28. Mehrabadi, M.M., Nemat-Nasser, S., Oda, M.: On statistical description of stress and fabric in granular materials. *Int. J. Numer. Anal. Methods Geomech.* **6**, 95–108 (1982). <https://doi.org/10.1002/nag.1610060107>
29. Oda, M.: Fabric tensor and its geometrical meaning. In: Introduction to mechanics of granular materials (1999)
30. Bathurst, R.J., Rothenburg, L.: Investigation of micromechanical features of idealized granular assemblies using DEM. *Eng. Comput.* **9**(2), 199–210 (1992)
31. Bathurst, R.J., Rothenburg, L.: Observations on stress-force-fabric relationships in idealized granular materials. *Mech. Mater.* **9**(1), 65–80 (1990)
32. Rothenburg L.: Micromechanics of idealized granular systems. Ph.D. Dissertation, Carleton University, Ottawa (1982)
33. Rothenburg, L., Bathurst, R.J.: Analytical study of induced anisotropy granular materials in idealized. *Geotechnique* **39**, 601–614 (1989)
34. Christoffersen, J., Mehrabadi, M.M., Nemat-Nasser, S.: A micromechanical description of granular material behavior. *J. Appl. Mech.* **48**(2), 339–344 (1981)
35. Rothenburg, L., Selvadurai, A.P.S.: A micromechanical definition of the Cauchy stress tensor for particulate media. In: Mechanics of structured media, pp. 469–486 (1981)
36. Ouadfel, H., Rothenburg, L.: Stress–force–fabric relationship for assemblies of ellipsoids. *Mech. Mater.* **33**(4), 201–221 (2001)
37. Ma, G., Chang, X.L., Zhou, W., Ng, T.T.: Mechanical response of rockfills in a simulated true triaxial test: a combined FDEM study. *Geomech. Eng.* **7**(3), 317 (2014)
38. Zhou, W., Liu, J., Ma, G., Yuan, W., Chang, X.L.: Macroscopic and microscopic behaviors of granular materials under proportional strain path: a DEM study. *Int. J. Numer. Anal. Methods Geomech.* **40**(18), 2450–2467 (2016)
39. Zhou, W., Yang, L., Ma, G., Chang, X., Lai, Z., Xu, K.: DEM analysis of the size effects on the behavior of crushable granular materials. *Granul. Matter* (2016). <https://doi.org/10.1007/s10035-016-0656-7>
40. Zhou, W., Wu, W., Ma, G., Huang, Y., Chang, X.L.: Study of the effects of anisotropic consolidation on granular materials under complex stress paths using the DEM. *Granul. Matter* **19**(4), 76 (2017)
41. Kloss, C., Goniva, C.: LIGGGHTS User Manual. (2014). <https://www.cfdem.com/media/DEM/docu/Manual.html>
42. Jop, P., Forterre, Y., Pouliquen, O.: A constitutive law for dense granular flows. *Nature* **441**, 727–730 (2006). <https://doi.org/10.1038/nature04801>
43. Wang, J., Dove, J.E., Gutierrez, M.S.: Discrete-continuum analysis of shear banding in the direct shear test. *Geotechnique* (2007). <https://doi.org/10.1680/geot.2007.57.6.513>
44. Oda, M., Konishi, J.: Rotation of principal stresses in granular material during simple shear. *Soils Found.* **14**(4), 39–53 (1974)
45. Thornton, C.: A DEM comparison of different shear testing devices. In: Powders and grains, pp. 183–190 (2001)
46. Xiao, Y., Sun, Y., Liu, H., et al.: Critical behaviors of a coarse granular soil under generalized stress conditions. *Granul. Matter* **18**, 1–13 (2016)
47. Xiao, Y., Liu, H., Ding, X., et al.: Influence of particle breakage on critical state line of rockfill material. *Int. J. Geomech.* **16**(1), 04015031 (2016)
48. Zhao, J., Guo, N.: Unique critical state characteristics in granular media considering fabric anisotropy. *Géotechnique* **63**(8), 695 (2013)
49. Behringer, R., Veje, C., Carolina, N.: Stress Fluctuations in a 2D granular Couette experiment: a continuous transition. *Phys. Rev. Lett.* **10**, 10 (1999). <https://doi.org/10.1103/PhysRevLett.82.5241>
50. Thornton, C.: Numerical simulations of deviatoric shear deformation of granular media. *Géotechnique* **50**, 43–53 (2000). <https://doi.org/10.1680/geot.2000.50.1.43>
51. Alonso-Marroquín, F., Luding, S., Herrmann, H.J., Vardoulakis, I.: Role of anisotropy in the elastoplastic response of a polygonal packing. *Phys. Rev. E Stat. Nonlinear Soft Matter Phys.* **71**, 10 (2005). <https://doi.org/10.1103/PhysRevE.71.051304>
52. Silbert, L.E., Ertaş, D., Grest, G.S., Halsey, T.C., Levine, D.: Analogies between granular jamming and the liquid-glass transition. *Phys. Rev. E Stat. Phys. Plasmas Fluids Relat. Interdiscip. Top.* **65**, 4 (2002). <https://doi.org/10.1103/PhysRevE.65.051307>
53. Radjai, F., Wolf, D.E., Jean, M., Moreau, J.-J.: Bimodal character of stress transmission in granular packings. *Phys. Rev. Lett.* **80**, 61–64 (1998). <https://doi.org/10.1103/PhysRevLett.80.61>
54. Iikawa, N., Bandi, M.M., Katsuragi, H.: Sensitivity of granular force chain orientation to disorder-induced metastable relaxation. *Phys. Rev. Lett.* **116**, 1–5 (2016). <https://doi.org/10.1103/PhysRevLett.116.128001>
55. Peters, J.F., Muthuswamy, M., Wibowo, J., Tordesillas, A.: Characterization of force chains in granular material. *Phys. Rev. E Stat. Nonlinear Soft Matter Phys.* **72**, 1–8 (2005). <https://doi.org/10.1103/PhysRevE.72.041307>
56. Matuttis, H.G., Luding, S., Herrmann, H.J.: Discrete element simulations of dense packings and heaps made of spherical and non-spherical particles. *Powder Technol.* **109**(1–3), 278–292 (2000)
57. Oron, G., Herrmann, H.J.: Exact calculation of force networks in granular piles. *Phys. Rev. E Stat. Phys. Plasmas Fluids Relat. Interdiscip. Top.* **58**, 2079–2089 (1998). <https://doi.org/10.1103/PhysRevE.58.2079>
58. Campbell, C.S.: A problem related to the stability of force chains. *Granul. Matter* **5**, 129–134 (2003). <https://doi.org/10.1007/s10035-003-0138-6>
59. Behringer, R., Howell, D., Kondic, L., Tennakoon, S., Veje, C.: Predictability and granular materials. *Phys. D Nonlinear Phenom.* **133**, 1–17 (1999). [https://doi.org/10.1016/S0167-2789\(99\)00094-9](https://doi.org/10.1016/S0167-2789(99)00094-9)
60. Radjai, F., Jean, M., Moreau, J.J., Roux, S.: Force distributions in dense two-dimensional granular systems. *Phys. Rev. Lett.* **77**, 274–277 (1996). <https://doi.org/10.1103/PhysRevLett.77.274>
61. Makse, H.A., Johnson, D.L., Schwartz, L.M.: Packing of compressible granular materials. *Phys. Rev. Lett.* **84**, 4160–4163 (2000). <https://doi.org/10.1103/PhysRevLett.84.4160>
62. O’Hern, C.S., Langer, S.A., Liu, A.J., Nagel, S.R.: Force distributions near jamming and glass transitions. *Phys. Rev. Lett.* **86**, 111–114 (2001). <https://doi.org/10.1103/PhysRevLett.86.111>
63. Danylenko, V.A., Mykulyak, S.V., Polyakovskiy, V.O., Kulich, V.V., Oleynik, I.I.: Force distribution in a granular medium under dynamic loading. *Phys. Rev. E* **96**, 1–6 (2017). <https://doi.org/10.1103/PhysRevE.96.012906>
64. Blair, D.L., Mueggenburg, N.W., Marshall, A.H., Jaeger, H.M., Nagel, S.R.: Force distributions in three-dimensional granular assemblies: effects of packing order and interparticle friction. *Phys. Rev. E Stat. Nonlinear Soft Matter Phys.* **63**, 413041–413048 (2001). <https://doi.org/10.1103/PhysRevE.63.041304>

65. Baxter, G.W., Leone, R., Behringer, R.P.: Experimental test of time scales in flowing sand. *Eur. Lett.* **21**, 569–574 (1993)
66. Hurley, R.C., Hall, S.A., Andrade, J.E., Wright, J.: Quantifying interparticle forces and heterogeneity in 3D granular materials. *Phys. Rev. Lett.* (2016). <https://doi.org/10.1103/PhysRevLett.117.098005>
67. Chikkadi, V., Schall, P.: Nonaffine measures of particle displacements in sheared colloidal glasses. *Phys. Rev. E* **85**(3), 031402 (2012)
68. Alexander, S.: Amorphous solids: their structure, lattice dynamics and elasticity. *Phys. Rep.* **296**(2–4), 65–236 (1998)
69. Wyart, M., Nagel, S.R., Witten, T.A.: Geometric origin of excess low-frequency vibrational modes in weakly connected amorphous solids. *Europhys. Lett.* **72**(3), 486 (2005)
70. O’hern, C.S., Silbert, L.E., Liu, A.J., Nagel, S.R.: Jamming at zero temperature and zero applied stress: the epitome of disorder. *Phys. Rev. E* **68**(1), 011306 (2003)
71. Falk, M.L., Langer, J.S.: Dynamics of viscoplastic deformation in amorphous solids. *Phys. Rev. E* **57**(6), 7192 (1998)
72. Guo, N., Zhao, J.: Local fluctuations and spatial correlations in granular flows under constant-volume quasistatic shear. *Phys. Rev. E Stat. Nonlinear Soft Matter Phys.* **89**, 042208 (2014)
73. Goldenberg, C., Tanguy, A., Barrat, J.L.: Particle displacements in the elastic deformation of amorphous materials: local fluctuations vs. non-affine field. *EPL (Europhys. Lett.)* **80**(1), 16003 (2007)
74. Chikkadi, V., Mandal, S., Nienhuis, B., Raabe, D., Varnik, F., Schall, P.: Shear-induced anisotropic decay of correlations in hard-sphere colloidal glasses. *EPL (Europhys. Lett.)* **100**(5), 56001 (2012)
75. Chen, D., Semwogerere, D., Sato, J., Breedveld, V., Weeks, E.R.: Microscopic structural relaxation in a sheared supercooled colloidal liquid. *Phys. Rev. E* **81**(1), 011403 (2010)

Publisher’s Note Springer Nature remains neutral with regard to jurisdictional claims in published maps and institutional affiliations.